

PCCP

Accepted Manuscript



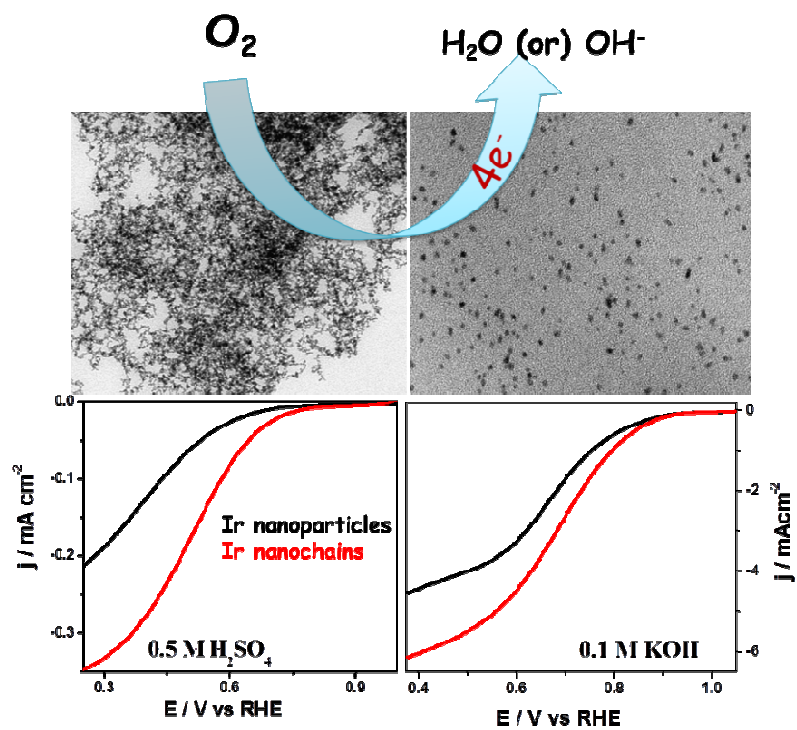
This is an *Accepted Manuscript*, which has been through the Royal Society of Chemistry peer review process and has been accepted for publication.

Accepted Manuscripts are published online shortly after acceptance, before technical editing, formatting and proof reading. Using this free service, authors can make their results available to the community, in citable form, before we publish the edited article. We will replace this *Accepted Manuscript* with the edited and formatted *Advance Article* as soon as it is available.

You can find more information about *Accepted Manuscripts* in the [Information for Authors](#).

Please note that technical editing may introduce minor changes to the text and/or graphics, which may alter content. The journal's standard [Terms & Conditions](#) and the [Ethical guidelines](#) still apply. In no event shall the Royal Society of Chemistry be held responsible for any errors or omissions in this *Accepted Manuscript* or any consequences arising from the use of any information it contains.

Oxygen reduction on Ir nanoparticles and nanochains in acidic and alkaline media



Morphology Dependent Electrocatalytic Activity of Ir Nanostructures Towards Oxygen Reduction

Kalapu Chakrapani and Srinivasan Sampath*
Department of Inorganic and Physical chemistry
Indian Institute of Science, Bangalore, India

* For correspondence

E-mail: sampath@ipc.iisc.ernet.in
Tel: +91 80 2293 3315; Fax: +91 80 2360 6867

Abstract

Iridium nanostructures with different morphologies are synthesized by a simple, environmentally friendly approach in aqueous media under mild conditions. The morphology dependent electrocatalytic activity of Ir nanochains and nanoparticles towards oxygen reduction reaction (ORR) has been demonstrated in both acidic and alkaline media. Comparative electrochemical studies reveal that nanochains exhibit significantly enhanced ORR activities in both acidic and alkaline media as compared with nanoparticles, as a result of continuous structure of interconnected particles. The mechanism of oxygen reduction on Ir nanostructures predominantly follows a four-electron pathway in alkaline and acidic solutions. Excellent stability and good selectivity towards methanol tolerance is reported.

Introduction

Electrochemical reduction of oxygen (ORR) on new and novel electrode surfaces is important especially towards applications in the areas of batteries, fuel cells, air cathodes and also for many industrial electrochemical reactions such as chlor-alkali process.¹⁻⁴ Most of the fuel cells are designed to utilize the electrochemical reduction of oxygen as the cathode reaction to balance the anodic oxidation of fuels.⁵ The reduction kinetics of oxygen on most of the electrodes is quite slow and it has been reported to be 6-order slower than the kinetics of anodic oxidation of alcohols.⁶ This makes ORR a limiting reaction for the performance of energy systems. It is necessary to find catalysts to improve the kinetics of ORR.⁷ ORR can proceed in two pathways depending on the nature of the catalyst, pH of the solution etc. (i) direct 4-electron conversion to water and (ii) indirect pathway leading to the formation of H_2O_2 as an intermediate via 2 electron process.^{8,9} Platinum is known to be the most effective electrocatalyst for polymer electrolyte fuel cells especially for ORR.^{10,11} Due to limited abundance and prohibitive cost and also its ability to react with fuels that cross-over to the cathode (termed as 'cross-over effect'), there is constant search for alternates to Pt.¹² Fuel cross-over is a major issue in direct alcohol fuel cells resulting in fuel permeation through polymer electrolyte membrane into the cathode compartment generating a mixed potential that affects the efficiency of fuel cells.¹³ This can be overcome by choosing electrocatalysts that are tolerant to the presence of alcohols during ORR. Iridium has been reported to help in the dissociation of oxygen, based on DFT calculations¹⁴ and hence Ir-based nanostructures can be good catalysts for ORR.

Iridium is one of the stable elements that is highly resistive to corrosion.¹⁵ Iridium has been studied as electrocatalysts for various electrochemical reactions, including small molecule oxidation.¹⁶⁻¹⁹ Bimetallic structures of Ir with different metals such as vanadium, Pt supported on carbon has been studied for ORR in acidic media.²⁰⁻²³ Further, iridium selenides of different compositions are also used to effect ORR.²⁴⁻²⁵ However, there is no previous report of using size and shape dependent activity of Ir nanostructures for ORR activity. In the present studies, we explore the use of interconnected Ir nanochains synthesized under mild conditions as electrocatalysts for ORR in both acidic and alkaline conditions. Methanol tolerance studies have also been carried out.

Experimental section

IrCl_3 was obtained from Alfa Aesar, Germany. Sodium borohydride and ascorbic acid were obtained from Polysales, India. 40 wt% Pt/ C was received from Arora Matthey, India.

Synthesis of Ir nanochains

Iridium nanochain-like structures were prepared using sodium borohydride as reducing agent and ascorbic acid (AA, which is biocompatible) as capping agent under aqueous medium.²⁶ In a typical synthesis, an aqueous IrCl_3 solution (1 mM) was stirred in the presence of an 2 mM ascorbic acid followed by the addition of freshly prepared sodium borohydride solution (20 mg in 10 mL water) and the mixture was heated at 80 °C in air under magnetic stirring for 6 hours and cooled down to room temperature.

During the reaction, the colour of the solution changed from light pale yellow to light brown colour. The resulting colloid was precipitated with ethanol and acetone (1:1) mixture and subsequently washed to remove excess capping agent.

Synthesis of Ir nanoparticles

Ir nanoparticles were prepared using polyvinylpyrrolidone (PVP) as the capping agent. Briefly 1 mM IrCl_3 and 4 mM PVP was dissolved in water followed by the addition of freshly prepared sodium borohydride solution (20 mg in 10 mL of water) and the mixture was stirred at 80°C for 2 hours and cooled down to room temperature. As explained in the results and discussion section, the formation of AA capped nanochains pass through the particle stage at short time intervals. Hence, Ir nanoparticles were also synthesized using AA as the capping agent by freezing the reaction mixture after 10 minutes of the reaction.

Physicochemical characterization

The as-prepared Ir nanostructures are characterized using various physicochemical techniques. Morphological information was obtained using transmission electron microscopy (TEM, JEOL 2100F) operated at 200 kV equipped with EDAX and selective area electron diffraction (SAED) accessories. The sample for TEM studies was prepared by drop-casting ethanolic dispersions of the sample onto holey carbon grids. Phase identification of the material was carried out using XRD (x-ray diffraction technique, Panalytical, Netherlands) equipped with graphite-monochromatized Cu-K α radiation source.

Electrochemical characterization

All the electrochemical measurements were carried out using CHI 660A electrochemical analyzer (CH instruments, TX, USA) with a conventional three electrode assembly. Working electrodes for ORR were fabricated as follows. Briefly, 3 mg of catalyst (Ir nanostructures) was dispersed in 1 mL water followed by the addition of 10 μL of nafion solution. The mixture was sonicated to obtain a homogeneous dispersion and 5 μL aliquot of the dispersion was uniformly spread onto polished glassy carbon (GCE) electrode of 3 mm diameter. The exact loading of Ir present on the working electrode based on the volume used is 210 $\mu\text{g}/\text{cm}^2$. The electrode was dried under ambient conditions and used for electrochemical studies. Ir modified GCE was used as the working electrode and large area Pt foil as the auxiliary electrode. Saturated calomel electrode (SCE) and mercury/mercuric oxide (Hg/HgO, 1M KOH) electrodes were used as reference electrodes in acidic and alkaline media, respectively. The reference electrodes are calibrated with respect to RHE²⁷ and are given in supporting information. ORR studies were performed in 0.5 M H_2SO_4 and 0.1 M KOH solutions by saturating the electrolyte with high pure O_2 gas for 30 minutes.

The currents observed were normalized with respect to the electrochemical active area. Electrochemical active surface area (ECSA) was determined using cyclic voltammetry in N_2 saturated 0.5 M H_2SO_4 solution by sweeping the potential from -0.3 V to 0.8 V vs. SCE at a scan rate of 0.05 V/s. The hydrogen adsorption/desorption region was used to obtain ECSA by assuming a charge of 0.22 mC/cm^2 for the monolayer coverage.^{15,18} Rotating disc electrode (RDE) measurements were carried out using RDE system from Pine instruments, USA (AFMSRCE) coupled with a potentiostat. All electrochemical experiments were carried out in a glass cell with provision for gas

purging. Commercial GC electrodes (3 mm diameter) were used for RDE studies, the surface of which was coated with the catalyst material.

Results and discussion

Figure 1 shows the TEM images of Ir nanostructures as-prepared using ascorbic acid (AA) and polyvinylpyrrolidone (PVP) as capping agents. It is clearly observed that the nanoparticles are connected together in the presence of AA to form extended interconnected Ir nanochains with different branches. At low magnifications, the structures are observed to be chain-shaped interconnected nanoparticles while at high magnifications, the nanochains are observed to be consisting of individual nanoparticles of size 3.0 ± 0.3 nm that are in close proximity to each other. The chain formation is monitored quantitatively by recording TEM images at different time intervals of the growth process. It is observed that nanoparticles are formed at initial stages as shown in figure S1 (Supporting Information) and these particles reach their equilibrium size and further self-assemble in the presence of polyfunctional capping agent, AA. Figure S2 (Supporting Information) shows the high resolution TEM image of nanochains, from which lattice fringes are resolved with lattice spacing determined to be 2.25 \AA that corresponds to the (111) plane of fcc Ir. Based on the above observations, it is clear that polyfunctional capping molecules play an important role in the formation of assemblies of nanoparticles.²⁸ Figure 1b shows the spherical Ir nanoparticles formed in the presence of PVP as the capping agent. The particle size determined from TEM images is (2.5 ± 0.4) nm. X-ray diffraction patterns are used to examine the crystallinity and phase purity of nanostructures and are shown in figure 1c and 1d. As shown in

figure 1c, nanochains show dominant diffractions observed at 2θ values of 40.9, 47.2, 69.1 and 83.6 degrees corresponding to (111), (200), (220) and (311) facets of Ir fcc structure while for nanoparticles, only broad peak at 40.9 degrees corresponding to (111) reflection is observed. The crystallite size determined from Scherrer equation using full width half maximum at the most intense (111) plane for nanochains and nanoparticles is ~ 3.4 and ~ 2.9 nm respectively which are in good agreement with the corresponding sizes observed in TEM analysis. The broad diffraction features are observed due to small crystallite size. X-ray photoelectron spectroscopy is employed to ascertain the chemical composition of as-prepared Ir nanostructures. Figure S3 (Supporting Information) shows the core-level deconvoluted Ir-4f spectra which show two pairs of doublets with binding energy values observed at 61.1 eV and 64.1 eV corresponding to Ir $4f_{7/2}$ and $4f_{5/2}$ levels with peak to peak separation of 3 eV. This confirms that the Ir is present in zero oxidation state. The weak intense doublet observed at high binding energies of 62.3 and 65.1 eV may be assigned to surface oxidized Ir corresponding to iridium oxide (IrO_2).

Oxygen reduction in acidic medium

Metal nanochains may act as good electrocatalysts where the network backbone enhances the structural stability and electronic conductivity.²⁹⁻³¹ Hence, it is interesting to explore the ORR activity on Ir nanostructures. The calibration of reference electrode is performed in hydrogen saturated 0.5 M H_2SO_4 and 0.1 M KOH solution using Pt foil as the working and counter electrodes, as shown in figure S4 (supporting information). Figure 2A shows the cyclic voltammograms of Ir nanochains and nanoparticles

synthesized using AA as the capping agent, in nitrogen saturated 0.5 M H₂SO₄ solution. It is clearly observed that both nanostructures show typical characteristic features of polycrystalline Ir for Ir oxide formation and reduction in the positive direction. Hydrogen adsorption and desorption are observed in the range of - 0.05 V to 0.25 V vs. RHE whereas Ir oxidation is observed in the range of 0.95 V and the corresponding reduction of Ir oxide is observed around 0.6 V vs. RHE.¹⁵ As compared to nanoparticles, nanochains exhibit well-defined adsorption peaks for hydrogen, possibly due to well-defined crystal facets. It should be pointed out that the hydrogen adsorption / desorption behaviour on Ir depends on the crystallographic plane exposed³² and the (111) plane is reported to show only increase in currents and not well-defined peak while other planes show different behaviour. In order to understand the role of capping agent for hydrogen adsorption behaviour, Ir nanoparticles prepared using AA and PVP as capping agents (particle sizes are similar, ~ 3.0 nm as given in the TEM images) are compared and the corresponding voltammograms are shown in figure S5 (supporting information). It is clear that the shape of the voltammograms is very similar. There is a slight difference in currents observed and this might be due to the base currents being different as well as any small difference in the particle size distribution. The electrochemical active surface area (ECSA) of the nanostructures is determined by integrating the charge passed during the hydrogen adsorption / desorption process after correcting for double layer charging currents and assuming the charge required to oxidize a monolayer of hydrogen on Ir to be 0.22 mC/cm⁻² (Q_{ref}).^{15,18} The obtained ECSA value for nanochains is 7.35 m²/g which is 2.5 times higher than that of particles (2.67 m²/g).

Electrochemical reduction of oxygen has been investigated in O₂ saturated 0.5 M H₂SO₄ solution and the typical polarization curves for nanochains and particles are shown in figure 2B. A peak observed at 0.59 V vs. RHE is due to oxygen reduction process.^{18,19} The peak currents vary linearly as a function of square root of scan rate indicating that the process is diffusion controlled (Figure S6, Supporting Information). As shown in figure 2B, the cathodic peak potential for ORR shifts to more positive values (0.59 V vs. RHE) in the case of nanochains as compared to nanoparticles (0.53 V vs. RHE) under identical experimental conditions. It should be noted that the Ir particles synthesized using AA and PVP capping agents show similar characteristics for ORR though the peak potential is slightly (15 mV) more positive for AA capped particles as compared to PVP capped Ir particles (Figure S5, Supporting Information). These observations reveal the higher electrocatalytic activity for nanochains as compared to that of nanoparticles. Rotating disc electrode (RDE) measurements are carried out to understand the activity and kinetics for ORR on Ir nanostructures and the measurements are carried out in linear potential scan mode at a scan rate of 0.005 V/s. Figure 3A shows the effect of rotation rate on the reduction currents for Ir nanochains. The currents increase as a function of rotation rate due to availability of large reactant flux near the electrode surface.³³ As compared to nanoparticles (Figure S7, Supporting Information), nanochains show positive onset potential shifts with concomitant increase in current density. The kinetic parameters are calculated by analyzing the RDE data based on Koutecky–Levich equation (equations 1 and 2).^{34,35}

$$\frac{1}{j} = \frac{1}{j_k} + \frac{1}{j_d} \quad (1)$$

$$\frac{1}{j} = -\frac{1}{(nFkC_0)} - \frac{1}{0.62 nFC_0 D_0^{2/3} \nu^{-1/6} \omega^{1/2}} \quad (2)$$

where j is the measured current density at different potentials, j_k and j_d are kinetic and diffusion current densities, respectively; n is the number of electrons transferred per O_2 molecule; k is the rate constant, F is Faraday constant ($96,500 \text{ C mol}^{-1}$); ω is the rotation rate (revolutions per second); C_0 is the bulk concentration of O_2 ($1.1 \times 10^{-6} \text{ mol per cc}$); D_0 is the diffusion coefficient ($1.4 \times 10^{-5} \text{ cm}^2/\text{s}$) and ν is the kinematic viscosity ($0.01 \text{ cm}^2/\text{s}$).³⁴

The K-L plots are constructed and data shown in figure 3B indicate linear variation of j^{-1} with $\omega^{-1/2}$ at different applied potentials. The values of n and k determined from the plots are shown in table 1. The number of electrons is determined to be close to four (~ 3.8) at potentials, from 0.5 V to 0.25 V (Figure 3B) suggesting that efficient pathway for direct reduction of oxygen to water is followed. Rate constants calculated at different applied potentials are also shown in table 1. It is clear that the nanochains show higher rate constant values than that of nanoparticles and the values are quite comparable with commercial Pt/C (Table 1). Figure 4A shows the comparison of polarization curves for ORR on Ir nanoparticles, nanochains and commercial Pt/C at a scan rate of 5 mV/sec at 1600 rpm. It is observed that the onset potential for ORR in acidic medium shifts by about 75 mV more positively in the case of nanochains as compared to particles. The comparative studies reveal that Ir nanochains show better efficiency in terms of both onset potential and also rate constant for ORR in 0.5 M H_2SO_4 than that of Ir nanoparticles.

The activity for ORR depends on the electrochemically active surface area, efficient active sites for adsorption of molecular oxygen and possibly surface defects present on the catalyst surface.³⁶⁻³⁹ It has been documented in the case of Pt nanochains that enhanced electrocatalytic activity towards ORR is due to the presence of (i) abundance of low index crystal faces, (ii) unique nanochain network structure that facilitates electron transport and resultant O₂ diffusion and (iii) few surface defect sites.^{29,36} Though speculative in this case, it is likely that the three are possible reasons for enhanced activity. We have earlier proposed in the case of one dimensional titanium carbide nanostructures that the adsorption characteristics are different as compared to that of nanoparticles resulting in the mechanism being different.³⁸ It has been shown based on density functional theory (DFT) calculations that there is an elongation of O-O bond length in the ORR intermediate species which results in the mechanism being different on one dimensional nanostructures as opposed to nanoparticles.³⁸ Similarly, the increased activity observed in the present studies on Ir nanochains is likely to be due to the (i) enhanced mass transport of oxygen and different adsorption characteristics enabled by unique morphology and (ii) abundance of low energy crystal facets such as Ir (111) and possibly different adsorption behavior of oxygen.

The Tafel plots are constructed on the basis of RDE data at 1600 rpm by polarizing the electrode at a very slow scan rate of 0.001 V s⁻¹. The Tafel slopes are determined (Figure 4B) at two different regions (table 2). In the low current density region, the values of Tafel slopes for Ir nanochains and particles are -67 mV and -76 mV per decade. At high current densities, the Tafel slopes are observed to be -142 mV and -159 mV per decade for nanochains and particles respectively. The Tafel slopes of

-60 mV and -120 mV are characteristics of ORR on bulk, polycrystalline Pt and Pd - based nanostructures.^{34,40,41} A change in slope has been attributed to a change from Temkin to Langmuir adsorption conditions as a consequence of adsorption of reaction intermediates. The Tafel slopes obtained in the case of Ir nanostructures suggests that the reaction mechanism is similar to that observed on Pt and Pd.

Fuel cross over from the anode to cathode compartment is a common problem encountered when liquid fuels like methanol and ethanol are used in the anodic compartment of fuel cells. This decreases the cell efficiency drastically.⁴² This problem can be overcome by using catalysts with high methanol tolerance and good selectivity towards oxygen reduction. The ORR activity of Ir nanochains in the presence of methanol is studied using voltammetry and *i-t* transients. Figure 5 shows the polarization curves for ORR activity on Ir nanostructures in the absence and presence of methanol respectively. As shown in figure 5A, the peak potential for ORR does not change after the addition of MeOH indicating high ORR activity for Ir nanochains in presence of methanol. The inactivity of Ir nanochains towards methanol oxidation is observed from cyclic voltammogram as well (Figure 5B). This is further demonstrated by successive additions of methanol during the measurement of *i-t* transient for ORR (Figure 5C). The ORR currents do not change even after the addition of 1.5 M of methanol, suggesting that Ir is inactive for methanol oxidation.

The durability of electrocatalytic materials is an important issue for practical applications and hence it is essential to explore the stability of Ir nanostructures.⁴³ The stability of Ir nanostructures is followed by applying potential sweeps between -0.05 V and 1.0 V in O₂ saturated 0.5 M H₂SO₄ at 25°C. After 200 cycles, the electrocatalytic

activity of Ir nanochains shows a very small shift of ~ 10 mV for ORR while in the case of nanoparticles, a shift of ~ 40 mV is observed (Figure 6). The Ir nanochains show long term durability as compared to nanoparticles. The structural evolution of nanostructures before and after potential cycling is investigated using TEM analysis. During potential cycling, Ir nanoparticles undergo Ostwald ripening to form large aggregates resulting in significant loss of electrocatalytic activity (Figure 7) as proposed earlier for Pt nanostructures.⁴⁴ However, in the case of Ir nanochains, the change in morphology and size of the particles after the durability test is not substantial while the nanoparticles undergo extensive agglomeration (Figure 7). Thus, the Ir nanochains show excellent electrocatalytic stability, superior activity and high methanol tolerance as compared to nanoparticles. The improved activity is likely to be due to interconnected structure that improves easy transport of electrons and possibly assists in the adsorption of intermediates as well.

Oxygen reduction in alkaline medium

Electrocatalytic activity of Ir nanostructures towards ORR in alkaline medium is not explored. Electrochemical behavior of Ir nanostructures in 0.1 M KOH solution (Figure S8, Supporting Information) shows characteristic features for hydrogen adsorption and desorption along with formation of Ir oxide and reduction. The H_2 adsorption and desorption is observed in the range of 0.15 to 0.35 V while the formation of Ir oxide is observed around 0.65 - 0.7 V. Reduction of Ir oxide is at 0.6 V vs. RHE. Ir nanochains exhibit well-defined hydrogen adsorption and desorption peaks. Figure 8 shows the typical polarization ORR curves for nanochains and particles in oxygen saturated 0.1 M KOH solution. It is clearly observed that the onset potential for ORR in

the case of nanochains is observed at 0.96 V and is shifted towards more positive values than that observed for nanoparticles (0.92 V). The peak currents vary linearly as the function of square root of scan rate suggesting diffusion controlled process (Figure S9, Supporting Information). Rotating disk electrode measurements are carried out in O₂ saturated 0.1 M KOH solution in order to calculate the kinetic parameters (Figure 9 and Figure S10, Supporting Information). The kinetic parameters are calculated based on the Koutecky-Levich equation as given before and the values used are, 1.1×10^{-6} mol per cc (for C₀), 1.4×10^{-5} cm²/s for D₀, and 0.01 cm²/s for ν .⁴⁵ The K-L plots at different potentials vary linearly as $1/i$ vs. $\omega^{-1/2}$ (Figure 9B). The kinetic parameters are given in table S1 (Supporting Information). The n value is found to be ~ 3.85 in both the cases suggesting 4 electron processes with water as the final product. The rate constant values at different potential are shown in table S1 (Supporting Information) for both nanoparticles and nanochains. It is observed that the rate constant is higher in the case of Ir nanochains than that of nanoparticles. Figure 10 shows the comparison of i-E polarization curves for ORR on Ir nanoparticles and Ir nanochains at a scan rate of 0.005 V/s and at a rotation rate of 1000 rpm. It is clear that the Ir nanochains show positive onset potentials as compared to that of Ir nanoparticles. There exist two different Tafel slopes at different potential regions as observed in acidic medium and also for Pt and Pd (Table S2, Supporting Information).^{34,40,46}

Conclusions

The electrocatalytic properties of two different morphologies of Ir towards oxygen reduction reactions in acidic and alkaline media are demonstrated. Enhanced electrocatalytic activity of Ir nanochains in acidic and alkaline solutions may be ascribed

to the unique continuous structure of interconnected nanoparticles and probably fast O₂ diffusion. The methanol tolerance property coupled with the possibility of four electron process may place Ir as a good candidate for fuel cell catalysts and also for metal-air batteries.

References

1. M. L. Debe, *Nature*, 2012, **486**, 43.
2. P. G. Bruce, S. A. Freunberger, L. J. Hardwick and J. M. Tarascon, *Nat. Mater.*, 2012, **11**, 19.
3. S. Guo, S. Zhang and S. Sun, *Angew. Chem. Int. Ed.*, 2013, **52**, 2.
4. W. Xiong, F. Du, Y. Liu, A. Perez, M. Supp, T. S. Ramakrishnan, L. M. Dai and L. Jiang, *J. Am. Chem. Soc.*, 2010, **132**, 15839.
5. J. Snyder, T. Fujita, M. W. Chen and J. Eelebancher, *Nat. Mater.*, 2010, **9**, 904.
6. J. S. Lee, S. T. Kim, R. Cao, N. S. Choi, M. Liu, K. T. Lee and J. Cho. *Adv. Energy Mater.*, 2011, **1**, 34.
7. Y. J. Wang, D. P. Wilkinson and J. Zhang, *Chem. Rev.*, 2011, **111**, 7625.
8. B. Fang, N. K. Chaudhari, M. S. Kim, J. H. Kim and J. S. Yu, *J. Am. Chem. Soc.*, 2009, **131**, 15330.
9. J. Chen, B. Lim, E. P. Lee and Y. Xia, *Nano Today*, 2009, **4**, 81.
10. H. Yano, J. M. Song, H. Uchida and M. Watanabe, *J. Phys. Chem. C*, 2008, **112**, 8372.
11. M. Subhramannia and V. K. Pillai, *J. Mater. Chem.*, 2008, **18**, 5858.
12. M. R. Gao, Q. Gao, J. Jiang, C. H. Cui, W. T. Yao and S. H. Yu, *Angew. Chem. Int. Ed.*, 2011, **50**, 4905.

13. M. Arenz, K. J. J. Mayrhofer, V. Stamenkovic, B. B. Blizanac, T. Tomoyuki, P. N. Ross, and N. M. Markovic. *J. Am. Chem. Soc.*, 2005, **127**, 6819.
14. J. K. Norskov, J. Rossmeisl, A. Logadottir, L. Lindqvist, J. R. Kitchin, T. Bligaard and H. Jonsson, *J. Phys. Chem. B*, 2004, **108**, 17886.
15. D. A. J. Rand and R. Woods, *J. Electroanal. Chem.*, 1974, **55**, 375.
16. V. Kiran, T. Ravikumar, N. T. Kalyanasundaram, S. Krishnamurthy, A. K. Shukla and S. Sampath, *J. Electrochem. Soc.*, 2010, **157**, B1201.
17. W. Du, Q. Wang, D. Saxner, N. A. Deskins, D. Su, J. E. Krzanowski, A. I. Frenkel and X. Teng, *J. Am. Chem. Soc.*, 2011, **133**, 15172.
18. Y. Zhang, H. Zhang, Y. Zhang, Y. Ma, H. Zhong and H. Ma, *Chem. Commun.*, 2009, 6589.
19. J. H. Shim, J. E. Kim, Y. B. Cho, C. Lee, Y. Lee, *Phys. Chem. Chem. Phys.* 2013, **15**, 15365.
20. J. S. Zheng, X. Z. Wang, J. L. Qiao, D. J. Yang, B. Li, P. Li and J. X. Maa, *Electrochem. Commun.* 2010, **12**, 27.
21. J. Qiao, R. Lin, B. Li, J. Ma and J. Liu, *Electrochim. Acta*, 2010, **55**, 8490.
22. K. A. Kuttiyiel, K. Sasaki, Y. M. Choi, D. Su, P. Liu and R. R. Adzic, *Energy Environ. Sci.*, 2012, **5**, 5297.
23. R. Loukrakpam, B. N. Wanjala, J. Yin, B. Fang, J. Luo, M. Shao, S. Protsailo, T. Kawamura, Y. Chen, V. Petkov and C. Z. Zhong, *ACS Catal.*, 2011, **1**, 562.
24. G. Liu and H. Zhang, *J. Phys. Chem. C*, 2008, **112**, 2058.
25. R. Zhang and W. Chen, *J. Mater. Chem. A*, 2013, **1**, 11457.
26. K. Chakrapani and S. Sampath, *Chem. Commun.*, 2014, **50**, 3061.

27. M.-R. Gao, Z.-Y. Lin, T.-T. Zhuang, J. Jiang, Y.-F. Xu, Y.-R. Zheng and S.-H. Yu, *J. Mat. Chem.* 2012, **22**, 13662.
28. K. Chakrapani and S. Sampath, *Chem. Commun.*, 2013, **49**, 6793.
29. J. Xu, G. Fu, Y. Tang, Y. Zhou, Y. Chen and T. Lu, *J. Mater. Chem.*, 2012, **22**, 13585.
30. C. Xu, Y. Liu, Q. Hao and H. Duan, *J. Mater. Chem. A*, 2013, **1**, 13542.
31. R. Z. Yang, J. Leisch, P. Strasser and M. F. Toney, *Chem. Mater.*, 2010, **22**, 4712.
32. N. Furuya and S. Koide, *Surf. Sci.*, 1990, **226**, 221.
33. V. Kiran, K. L. Nagashree and S. Sampath, *RSC Adv.*, 2014, **4**, 12057.
34. N. Alexeyeva, T. Laaksonen, K. Kontturi, F. Mirkhalaf, D. J. Schiffrin, and K. Tammaeveski, *Electrochem. Commun.*, 2006, **8**, 1475.
35. K. Moses, V. Kiran, S. Sampath and C. N. R. Rao, *Chem. Asian J.*, 2014, **9**, 838.
36. H. W. Liang, X. Cao, F. Zhou, C. H. Cui, W. J. Zhang and S. H. Yu, *Adv. Mater.*, 2011, **23**, 1467.
37. C. Koenigsmann, W. P. Zhou, R. R. Adzic, E. Sutter, and S. S. Wong, *Nano Lett.*, 2010, **10**, 2806.
38. V. Kiran, K. Srinivasu, and S. Sampath, *Phys. Chem. Chem. Phys.*, 2013, **15**, 8744.
39. S. Kondo, M. Nakamura, N. Maki and N. Hoshi, *J. Phys. Chem. C*, 2009, **113**, 12625.
40. H. Erikson, A. Sarapuu, N. Alexeyeva, K. Tammaeveski, J. S. Gollan and J. M. Feliu, *Electrochim. Acta*, 2012, **58**, 329.

41. C. Wang, M. Chi, D. Li, D. Strmcnik, D. van der Vliet, G. Wang, V. Komanicky, K. C. Chang, A. P. Paulikas, D. Tripkovic, J. Pearson, K. L. More, N. M. Markovic and V. R. Stamenkovic, *J. Am. Chem. Soc.*, 2011, **133**, 14396.
42. X. Zhao, M. Yin, L. Ma, L. Liang, C. Liu, J. Liao, T. Lu, and W. Xing, *Energy Environ. Sci.*, 2011, **4**, 2736.
43. S. M. Alia, G. Zhang, D. Kisailus, D. Li, S. Gu, K. Jensen and Y. Yan, *Adv. Funct. Mater.*, 2010, **20**, 3742.
44. Z. W. Chen, M. Waje, W. L. Li and Y. S. Yan, *Angew. Chem. Int. Ed.*, 2007, **46**, 4060.
45. J. Qiao, L. Xu, L. Ding, P. Shi, L. Zhang, R. Baker and J. Zhang, *Int. J. Electrochem. Sci.*, 2013, **8**, 1189.
46. L. Jiang, A. Hsu, D. Chu, and R. Chen, *J. Electrochem. Soc.*, 2009, **156**, B643.

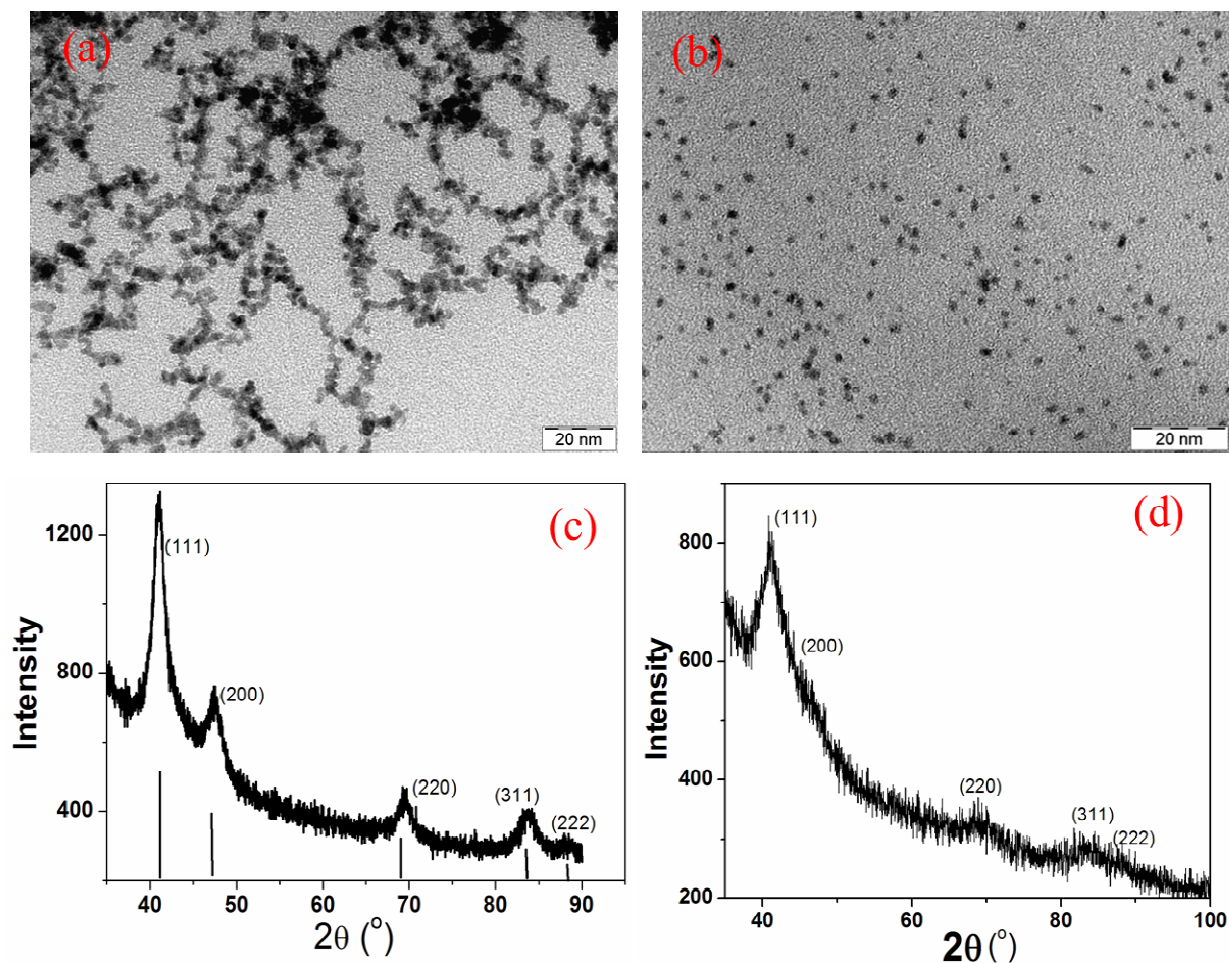


Figure 1: TEM images and corresponding X-ray diffraction patterns of (a, c) Ir nanochains and (b, d) Ir nanoparticles. The nanochains are synthesized using AA as the capping agent while nanoparticles are synthesized using PVP as the capping agent.

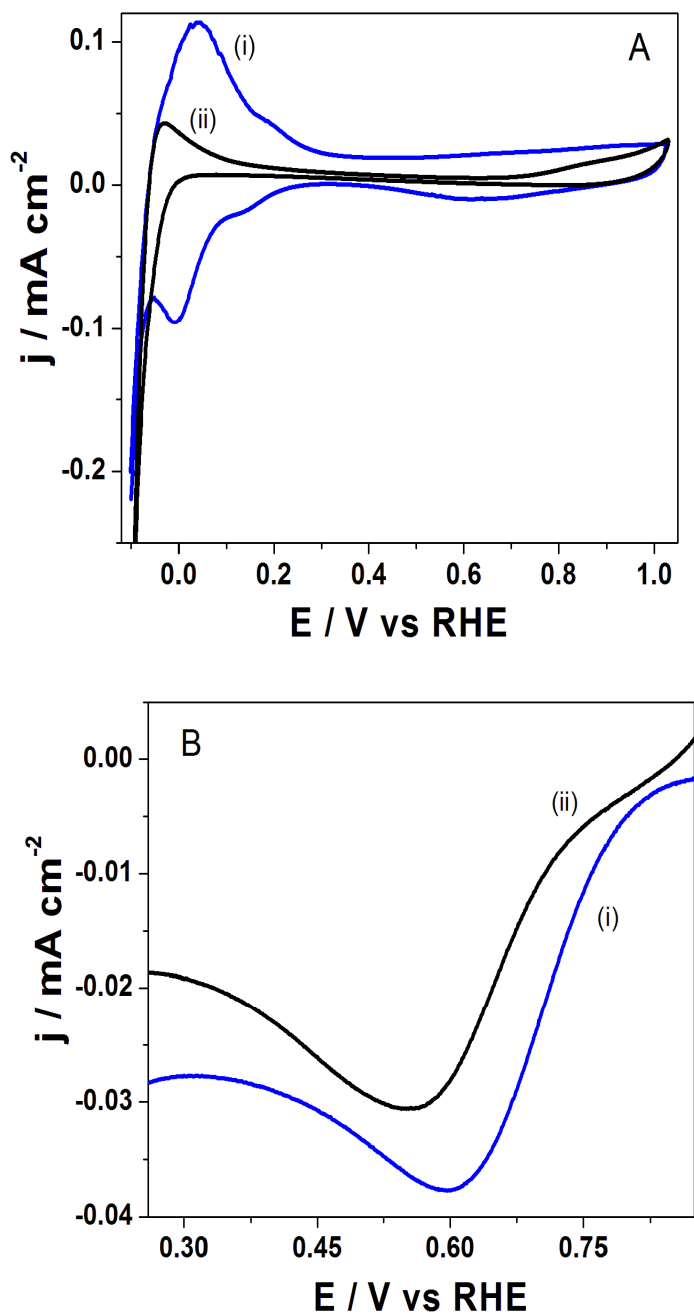


Figure 2: (A) Cyclic voltammograms of (i) Ir nanochains and (ii) Ir nanoparticles in N_2 saturated $0.5 \text{ M H}_2\text{SO}_4$ at a scan rate of 0.05 V/s and (B) Linear sweep voltammograms in O_2 saturated $0.5 \text{ M H}_2\text{SO}_4$ solution at a scan rate of 0.005 V/s . Loading of Ir used is $210 \mu\text{g}/\text{cm}^2$ on a GCE.

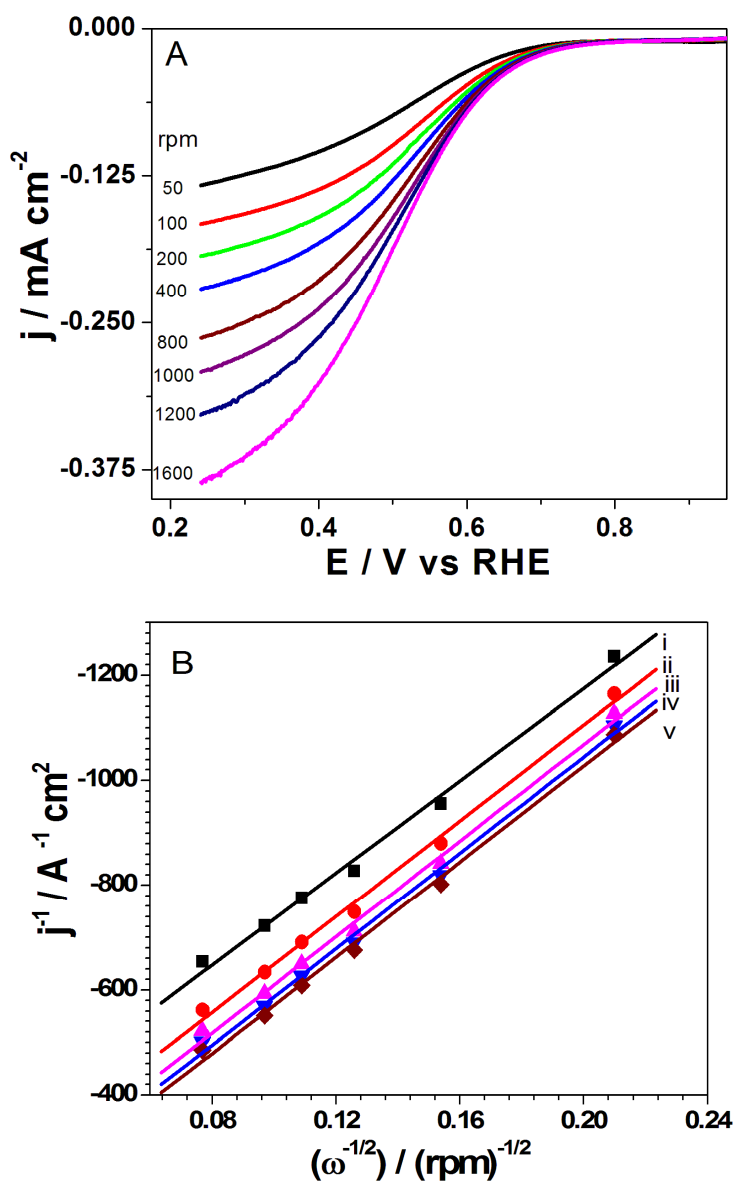


Figure 3: (A) Linear sweep voltammograms showing the effect of rotation rate on Ir nanochains. The scan rate used is 0.005 V/s. Electrolyte used is O₂ saturated 0.5 M H₂SO₄. (B) Koutecky-Levich plots for ORR on Ir nanochains at different applied DC potentials (i) 0.5 V; (ii) 0.45 V; (iii) 0.4 V; (iv) 0.35 V and (v) 0.25 V. Loading of Ir used is 210 μg/cm² on a GCE.

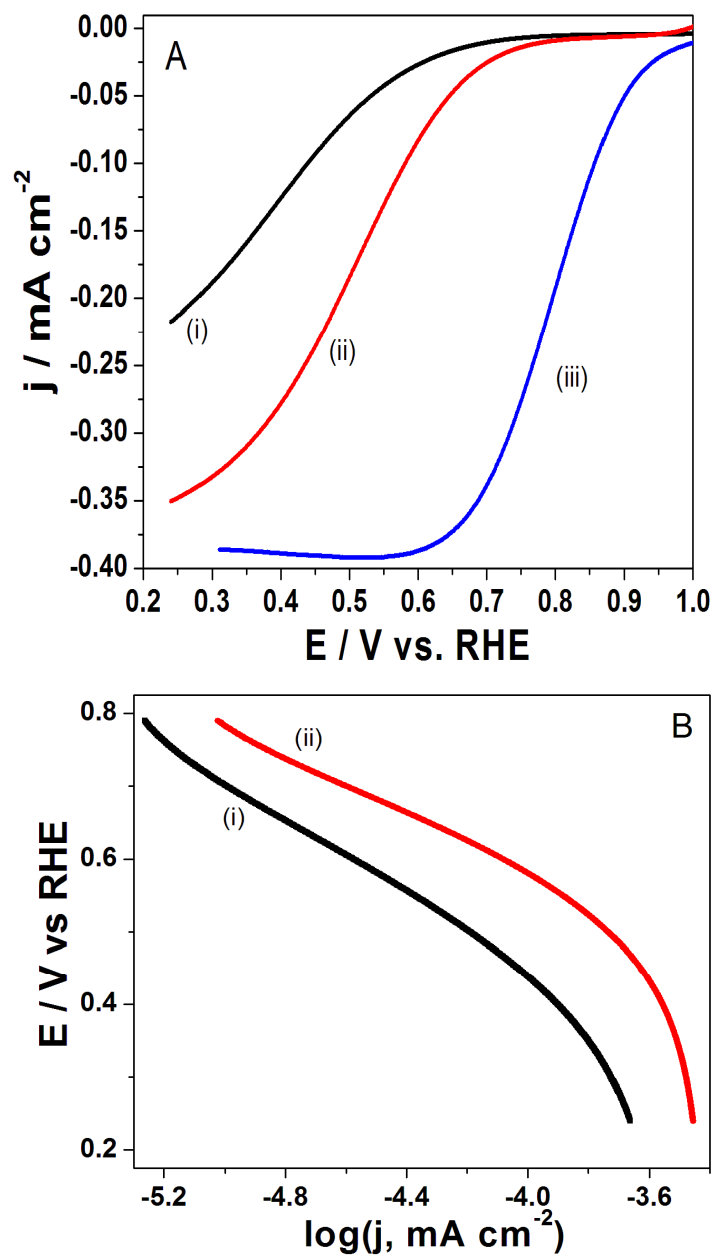


Figure 4: (A) Linear sweep voltammograms of (i) Ir nanoparticles, (ii) Ir nanochains and (iii) commercial Pt/C in O_2 saturated 0.5 M H_2SO_4 at a scan rate of 0.005 V/s. (B) Tafel plots for ORR on (i) Ir nanoparticle and (ii) Ir nanochain modified GCE in 0.5 M H_2SO_4 solution. Rotation rate used is 1600 rpm. Loading of Ir used is $210 \mu\text{g}/\text{cm}^2$ on a GCE.

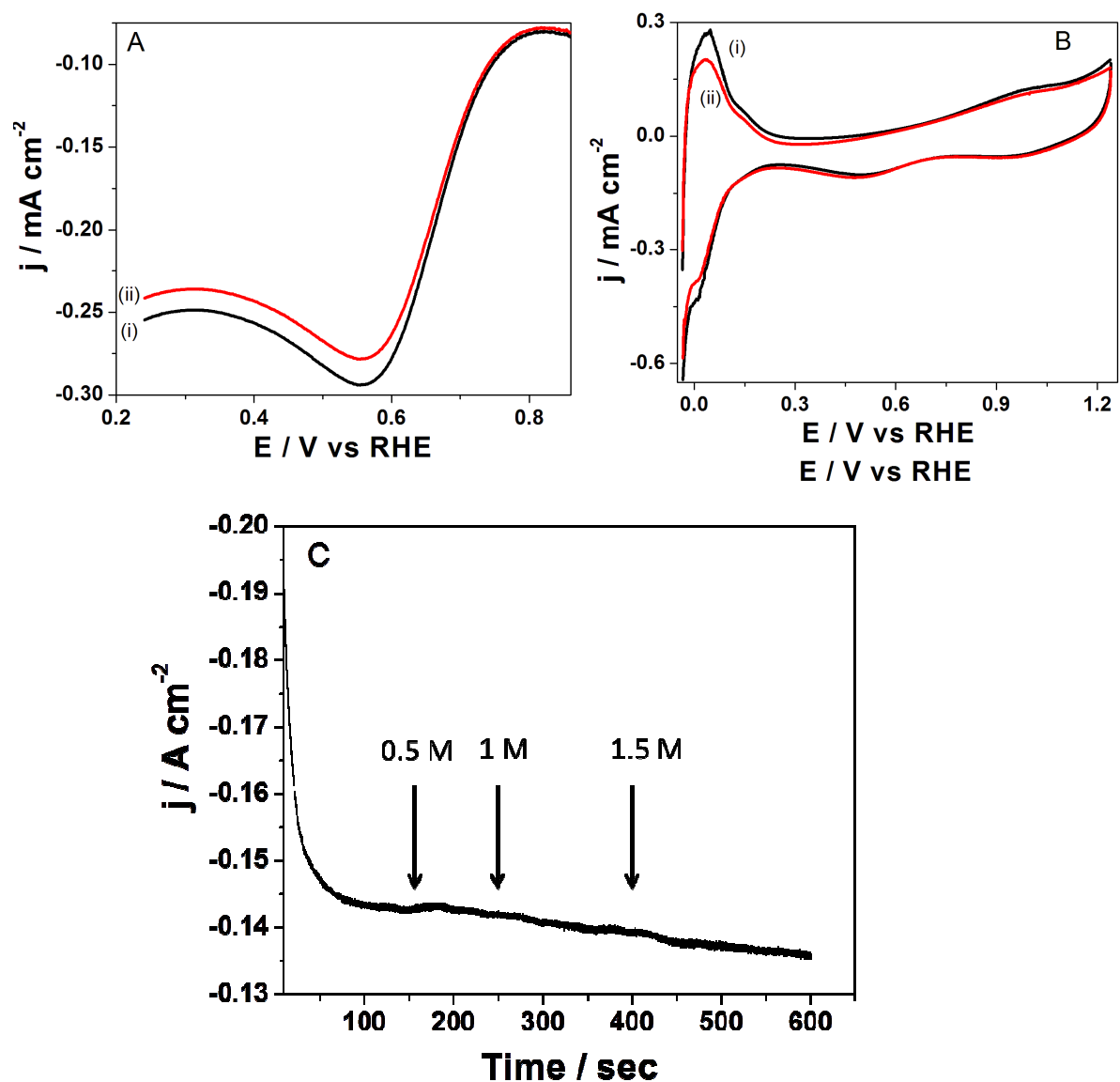


Figure 5: (A) Linear sweep voltammograms of Ir nanochains in O_2 saturated 0.5 M H_2SO_4 (i) before and (ii) after addition of 1M methanol at a scan rate of 0.005 V/s. (B) Cyclic voltammograms of ORR (i) before and (ii) after addition of 1M methanol; scan rate used is 0.05 V/s. (C) Chronoamperometric trace for ORR with the addition of different concentration of MeOH. The DC bias applied is 0.5 V. Arrows indicates the addition of methanol. Loading of Ir used is $210 \mu g/cm^2$ on a GCE.

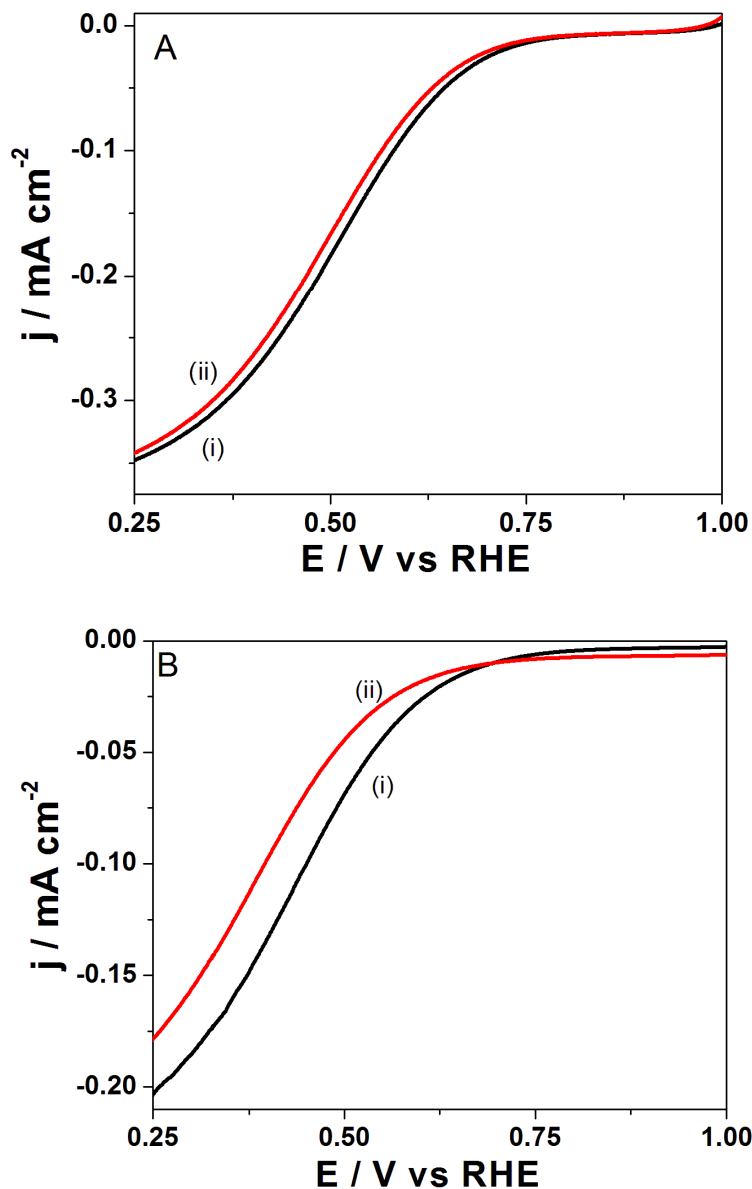


Figure 6: Oxygen reduction polarization curves observed for (A) Ir nanochains and (b) Ir nanoparticles (i) before and (ii) after 200 potential cycles, at scan rate of 0.005 V/s and at a rotation speed of 1600 rpm. Loading of Ir used is $210 \mu\text{g}/\text{cm}^2$ on a GCE.

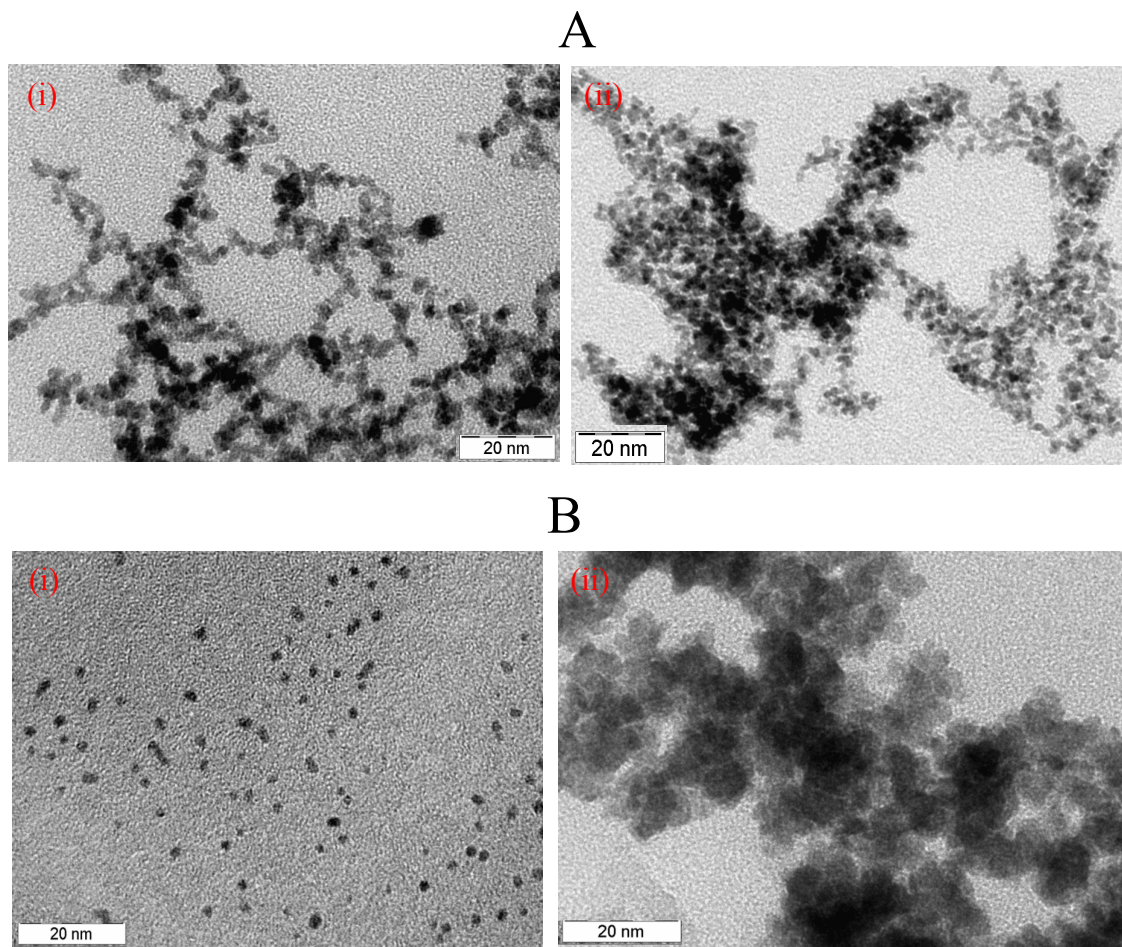


Figure 7: TEM images of (A) Ir nanochains and (B) Ir nanoparticles (i) before and (ii) after potential cycling for 200 cycles. Other conditions are as given in figure 6.

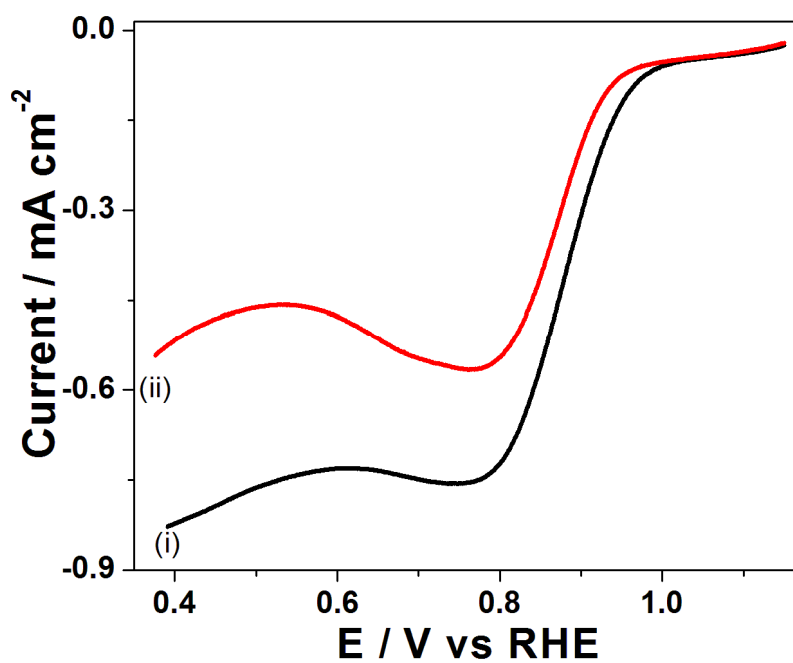


Figure 8: Linear sweep voltammograms of (i) Ir nanochains and (ii) Ir nanoparticles in O₂ saturated 0.1 M KOH solution at a scan rate of 0.005 V/s. Loading of Ir used is 210 $\mu\text{g}/\text{cm}^2$ on a GCE.

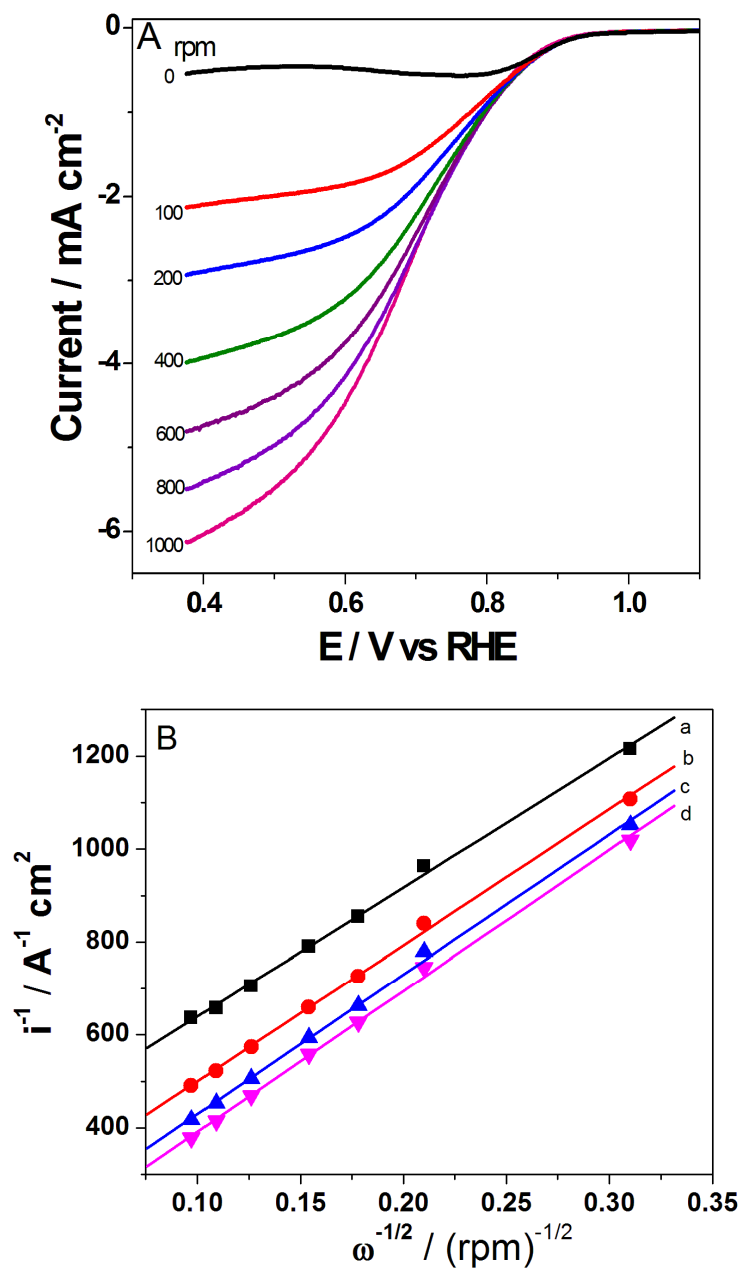


Figure 9: (A) Linear sweep voltammograms as a function of rotation rate in 0.1 M KOH solution on Ir nanochains; (B) corresponding K-L plots for ORR at different applied DC potentials (a) 0.65 V; (b) 0.6 V; (c) 0.55 V and (d) 0.5 V. Loading of Ir used is 210 $\mu\text{g}/\text{cm}^2$ on a GCE.

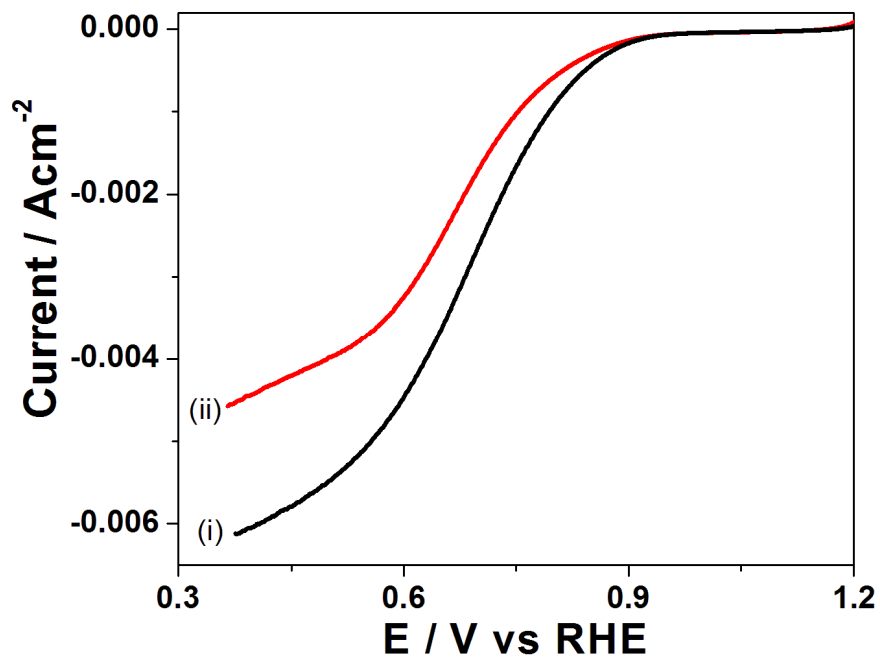


Figure 10: Linear sweep voltammograms of ORR on (i) Ir nanochains and (ii) Ir nanoparticles in O_2 saturated 0.1 M KOH solution at a rotation speed of 1000 rpm. Scan rate used is 0.005 V/s. Loading of Ir used is $210 \mu\text{g}/\text{cm}^2$ on a GCE.

Table 1: Number of electrons and rate constant values determined at different applied potentials on Ir nanoparticles, Ir nanochains and Pt/C for ORR in acidic medium.

E vs. RHE	Ir nanoparticles		Ir nanochains		Pt/C	
	n	k (cm/s)	n	k (cm/s)	n	k (cm/s)
0.5 V	3.6	0.0093	3.6	0.018	3.9	0.038
0.45 V	3.5	0.016	3.9	0.028	3.9	0.043
0.35 V	3.7	0.021	3.8	0.032	4.0	0.052
0.3 V	3.7	0.026	3.9	0.035	4.0	0.065

Table 2: Tafel slopes for ORR on Ir nanoparticles and Ir nanochains in 0.5 M H₂SO₄ at a rotation speed of 1600 rpm. Region-I and Region-II correspond to low and high current densities.

Catalyst	Tafel slope (mV/dec) Region-I	Tafel slope (mV/dec) Region-II	References
Ir nanoparticles	-76	-159	Present study
Ir nanochains	-67	-142	-do-
Pt	-62	-123	31
Pd	-63	-125	37